A study of the microstructural stability and defect evolution in an ODS Eurofer steel by means of Electron Microscopy and Positron Annihilation Spectroscopy

Pereira, V. S.M.; Schut, H.; Sietsma, J.

DOI
10.1016/j.jnucmat.2020.152398

Publication date
2020

Document Version
Final published version

Published in
Journal of Nuclear Materials

Journal of Nuclear Materials 540 (2020) 152398

Contents lists available at ScienceDirect

Journal of Nuclear Materials

journal homepage: www.elsevier.com/locate/jnucmat

A study of the microstructural stability and defect evolution in an ODS Eurofer steel by means of Electron Microscopy and Positron Annihilation Spectroscopy

V.S.M. Pereira [a, b, *], H. Schut [a], J. Sietsma [b]

[a] Delft University of Technology, Reactor Institute Delft, Faculty of Applied Sciences, The Netherlands
[b] Delft University of Technology, Materials Science and Engineering Department, Faculty of 3mE, The Netherlands

HIGHLIGHTS

- Mechanical alloying introduces a deformation state that persists in ODS steels even during annealing at 1200 K.
- Deformation state and Y-O based nanoparticles are likely responsible for microstructural instability at 1400 K.
- Positron annihilation results indicate that Y-O based nanoparticles are able to trap thermal-vacancy clusters.

ARTICLE INFO

Article history:
Received 3 December 2019
Received in revised form
6 July 2020
Accepted 9 July 2020
Available online 15 July 2020

Keywords:
Y-O based Nanoparticles
Martensitic ODS steel
Mechanical alloying
Deformation state
Thermal-vacancy clusters

ABSTRACT

An approach to improve the performance of steels for fusion reactors is to reinforce them with oxide nanoparticles. These can hinder dislocation and grain boundary movement and trap radiation-induced defects, thus increasing creep and radiation damage resistance. The present work investigates the thermal stability of the microstructure and the evolution of defects in a 0.3% Y_2O_3 dispersed Eurofer steel. Samples were annealed for 1 h under vacuum, from 600 K to 1600 K, followed by cooling inside the furnace. Electron Microscopy techniques and Vickers Hardness were used to characterize the microstructure and evaluate its thermal stability. Positron Annihilation Spectroscopy Doppler Broadening (PASDB) was used to monitor the evolution of defects, such as dislocations and vacancies, and their interaction with Y-O based nanoparticles. Several types of events take place simultaneously in the material, due to its initial deformation caused by mechanical alloying, the presence of oxide particles and austenitic phase transformation. Annealing up to 1000 K shows that the Y-O based nanoparticles keep the microstructure refined. Upon cooling from 1200 K (above A_{c3}), martensite forms with an equiaxed morphology, instead of the conventional lath form, due to the pinning of prior-austenite grain boundaries by the oxide nanoparticles. Annealing at 1400 K and 1600 K results in the progressive coarsening of Y-O based nanoparticles and their loss of ability to pin grain boundaries. PASDB shows that annealing up to 1200 K leads to an overall decrease in defect concentration, mainly due to recovery of dislocations. After annealing at 1400 K and 1600 K, PASDB indicates the formation of a different type of positron trap. The hypothesis is that, at these temperatures, clusters of thermal vacancies are trapped by the oxide nanoparticles, accumulating at their interfaces with the matrix and being retained in the material upon cooling to room temperature.

1. Introduction

Steels for nuclear applications must resist severe service conditions, like high temperatures (900 K–1300 K) and high neutron radiation doses. Also, in order to make nuclear power a safer and more environmentally friendly resource, a current requirement is to use reduced-activation alloying elements in the steel composition [1–7]. With this approach, irradiated structures that could take hundreds of years to reduce induced radioactivity should take no more than tens of years to reach a safe, low radiation

* Corresponding author. Delft University of Technology, Reactor Institute Delft, Faculty of Applied Sciences Mekelweg 15, 2629JB, Delft, The Netherlands.
E-mail address: v.marquespereira@tudelft.nl (V.S.M. Pereira).

https://doi.org/10.1016/j.jnucmat.2020.152398

level and then be recycled [8]. Reduced-activation steels have already been developed, like the Eurofer97, however they present poor resistance to radiation-induced creep and the service temperature is limited to 900 K, due to thermal instability of the microstructure. A way to improve these properties is to reinforce the steel with oxide nanoparticles, which are able to hinder dislocation and grain boundary movement and to trap radiation-induced defects [2–7,9].

The fabrication method of ODS steels is based on mechanical alloying, which enables the direct mixing of metallic and oxide powders, allowing a homogeneous distribution of oxide particles in the matrix [3,9–11]. The standard manufacturing powder-metallurgy route consists of the following steps: (1) gas atomization of a pre-alloy, (2) mechanical alloying of the metallic and oxide powders, (3) consolidation of the ODS alloy by extrusion, hot isostatic pressing or plasma-assisted sintering and (4) thermo-mechanical treatments like hot rolling, forging and cold rolling [3,7,9–11].

Pre-alloy powders of 9% Cr steels, like the Eurofer97 alloy, produced in step (1) have a microstructure formed by martensite laths. The oxide powders usually consist of crystallites with average diameters ranging from 20 to 100 nm [12,13]. After step (2), the mechanically-alloyed powders (MA powders) will present a very fine microstructure with an average grain size of tens of nanometers [14]. At this point, the martensite laths from the pre-alloyed powders transform into a more equiaxed structure with high density of dislocations (~10^{16} m^{-2}) [12,15]. Also, when milling ODS steel powders, the degree of refinement of the resultant microstructure will depend on the density of added oxide particles and on their chemical nature [13]. Cayron et al. [13] have observed the influence of both parameters on the microstructure of as-MA ODS Eurofer powders. In comparison with $MgAl_2O_4$, addition of Y_2O_3 leads to a finer microstructure. A higher content of Y_2O_3 causes a smaller grain size [13]. Additionally, Cayron et al. [13] conclude that $MgAl_2O_4$ does not dissolve in the steel matrix during mechanical alloying, while Y_2O_3 does [13]. Other authors [6,12,15–17] have also found that Y_2O_3 dissolves progressively in the matrix during mechanical alloying and re-precipitates as nanosized clusters in the other processing steps.

The chemical composition of the oxide clusters and their size distribution depend on the alloying elements added to the steel [6,12,14–17]. Kimura et al. [17] detected precipitation of Y_2O_3 and $YCrO_3$ in a 24% Cr ODS ferritic steel during annealing at 1200 K. A similar temperature was determined for a 13% Cr-3% Ti-Y_2O_3 steel and the re-precipitated clusters were identified as Y_2TiO_5 and $Y_2Ti_2O_7$ [16]. Brocq et al. [18] proposed a new process for producing Y_2O_3 ODS steels called reactive-inspired ball-milling. In this new process, YFe_3 and Fe_2O_3 oxide powders were milled with a Fe-14Cr-W-1Ti pre-alloy, and the authors have observed re-precipitation of oxide nanoclusters after milling and their growth during annealing at 1000 K for 1 h [16].

Commonly, during consolidation, the MA-powders are exposed to temperatures between 1100 K and 1400 K and, therefore, precipitation of Y-based oxide nanoclusters is likely to occur in this stage. It has been reported by different authors [10,12,13,15,19,20] that consolidated Y_2O_3-ODS steels present a microstructure composed of micrometric grains (3–15 μm) surrounded by smaller ones, with average diameter of hundreds of nanometers. The main reasons for this bimodal microstructure are the high deformation energy stored in the material, due to mechanical alloying, and the presence of oxide nanoparticles [12,15,19]. Briefly, the MA-powders have a high dislocation density and a large grain boundary area caused by the nano-sized grains. Therefore, they have a strong potential to go through microstructural alterations like recovery and recrystallization [14,21]. At the same time, the Y-based oxide nanoclusters exert a pinning force on dislocations and grain boundaries that hinder their movement (Zener pinning force). In this unstable state, regions of the material that have a low density of oxide nanoclusters might experience abnormal grain growth, which can be further assisted by an uneven temperature distribution during hot-processing steps [12,19].

In 9% Cr ODS steels there is an extra factor to consider when describing the consolidated and thermo-mechanically treated microstructures: the $\alpha \rightarrow \gamma$ phase transition and the γ decomposition upon cooling. Yamamoto et al. [20] observed with *in situ* X-Ray Diffraction, dilatometry and thermodynamic analyses that, irrespective of temperature, the transformation of ferrite into austenite is not complete in 9% Cr Y_2O_3-ODS steels. The Y-O based nanoclusters would favour ferrite retention by pinning α/γ interfaces [20]. It has also been reported that martensite laths do not form in 9% Cr Y_2O_3-ODS steels [13,20,22], even upon water quench. Again, a possible explanation is based on the Y-O nanoclusters, which would hinder the growth of austenite grains. In this way, austenitic grains would keep a nanometric average grain size and would not provide space for the growth of martensite laths during subsequent quenching [13,22].

The mechanisms involved in the microstructure evolution of ODS steels are complex, mainly because of the presence of Y-O based nanoclusters and the highly deformed structure obtained during mechanical alloying. Particularly for 9% Cr Y_2O_3-ODS steels, the nature of the consolidated microstructure is not clear, i.e., whether it is formed by ferrite, martensite or a combination of both or is affected by recrystallization and ferrite retention at high temperatures. Also, given that Y-O based nanoparticles play a role in radiation damage mechanisms, it is important to know how these particles interact with residual defects introduced during mechanical alloying or formed during any phase transition, prior to exposure to neutron radiation. Ortega et al. [23] have performed Positron Annihilation Lifetime and Coincidence Doppler Broadening measurements on consolidated samples of Eurofer and Y_2O_3-ODS Eurofer. The samples produced by mechanical alloying in Ar atmosphere and hot isostatic pressing were submitted to isochronal annealing treatments up to 1523 K. The authors have found that both steels absorb Ar atoms in the mechanical alloying stage, and these would facilitate the nucleation of thermal-vacancy clusters during later processing stages. In the Y_2O_3-ODS Eurofer steel, the oxide particles stimulate the nucleation of clusters of thermal vacancies and Ar atoms and keep them stable even after annealing at 1523 K [23].

Therefore, in the present paper we assess the microstructural stability, possible phase transformations and defect evolution in a 0.3% Y_2O_3 ODS Eurofer, after a series of annealing treatments. The aim is to characterize the microstructure after each annealing step and to identify processes like recovery, recrystallization and retention of ferrite. With the Positron Annihilation Spectroscopy Doppler Broadening method the interactions of defects, such as dislocations, thermal vacancies and possible residual Ar-vacancy clusters with the Y-O based nanoparticles are investigated.

2. Methodology

2.1. Material and heat treatments

The route used for fabrication of the 0.3% Y_2O_3 ODS Eurofer steel consisted of mechanical alloying, hot isostatic pressing, hot rolling, austenitization and tempering [24]. Table 1 presents the chemical composition of the steel, determined with X-Ray Fluorescence (heavy metallic elements) and Combustion Analysis (C and S). The samples used for the X-Ray Fluorescence (XRF) analysis were already annealed (description in the following paragraphs) and the

Table 1
Chemical composition of the steel, in weight%. The chemical composition of the present steel is slightly different from other ODS Eurofer steels, due to a lower Ta content.

ODS Eurofer	Fe	C	Cr	W	V	Mn	Ta	Y	O[a]	Si	S
	Bal.	0.11	9.18	1.01	0.19	0.39	Below detection limit (~0.01)	0.18	0.05	0.04	0.005

[a] Estimated value, assuming that all O added to the steel is in Y_2O_3 form.

ones used for C and S determination were in the as-received condition. Due to a limitation in the amount of material for the study, we could not perform Combustion Analysis for determination of the N and O contents. Finally, it should be noted that the Ta content is not displayed in Table 1. Ta is an alloying element commonly added to ODS and non-ODS Eurofer steels, in a typical content of 0.1 wt% [2]. It improves strength and the ductile-brittle transition temperature, due to the formation of TaC that contribute to microstructure refinement, especially in non-ODS Eurofer [2]. The Ta content measured by XRF in our material was below the detection limit (~0.01 wt%), therefore lower than the usual content for Eurofer.

The austenitization and tempering conditions used by the producer are unknown, therefore, in order to create a reference state, the material was initially austenitized at 1253 K for 0.5 h and tempered at 1033 K for 1.5 h. All samples had dimensions of $12 \times 12 \times 0.3$ mm^3, prior to the creation of the reference state, and were cut from the top surface of the original plate, at aleatory positions along the thickness of the plate. The treatments described were done in a resistant heating furnace built at the Reactor Institute Delft, under a low pressure of 10^{-7} mbar. In this furnace, the average heating rates that can be achieved vary between 0.6 and 2 K s^{-1}. The cooling was always made inside the furnace, at the same pressure of 10^{-7} mbar, by switching off its power supply. The cooling rate in this condition is not constant and depends on the temperature difference between the sample and the environment.

Next, the samples were further heat treated in the same furnace and vacuum condition for 1 h, at different temperatures: 600 K, 800 K, 1000 K, 1200 K, 1400 K and 1600 K. Again, the cooling took place inside the furnace. Fig. 1 shows the temperature profile for the sample treated at 1600 K, in order to illustrate the non-constant cooling behaviour. The data displayed in Fig. 1 was measured during the process and we can see a cooling time of 10 min between 1050 K and 750 K, which is a temperature range critical for phase transformations, leading to an average cooling rate of 0.5 K s^{-1}.

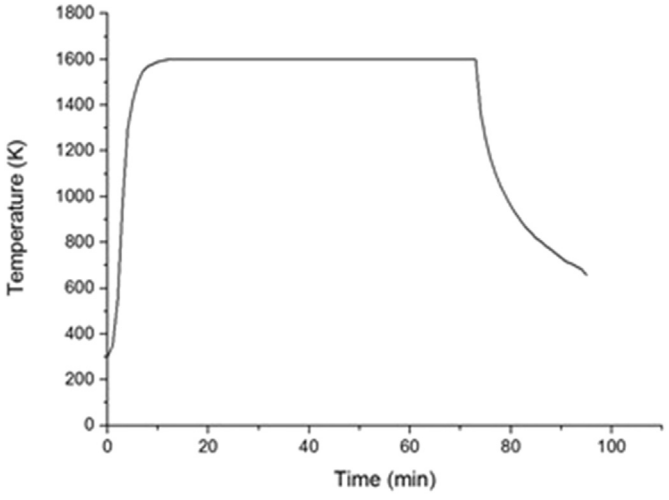

Fig. 1. Thermal cycle of sample annealed at 1600 K, to show the cooling rate induced by switching-off the furnace.

In order to have a reference for the phase transformations that can occur in the material, the Fe-Cr equilibrium diagram for the non-ODS Eurofer steel was calculated using Thermo-Calc version 2018a. The alloy composition considered and database selected were, respectively, Fe-0.1C-9.18Cr-1.070W-0.196V and TCFE9: Steels/Fe-alloys v9.0.

The transformation temperatures of the ODS Eurofer steel were determined experimentally using a Bähr DIL805A/D dilatometer. A sample in the reference state was heated up to 1573 K, at a heating rate of 1 K s^{-1}, maintained at this temperature for 5 min and finally cooled down by switching off the heating power of the dilatometer, inducing an approximate cooling rate of 6 K s^{-1} between 1050 K and 750 K.

2.2. Methods

2.2.1. Microstructural characterization

Scanning Electron Microscopy (SEM), Energy Dispersive X-Ray Spectroscopy (EDS) and Electron Backscattered Diffraction (EBSD) were used to characterize the microstructure of the 0.3% Y_2O_3 ODS Eurofer steel in the reference state and after annealing treatments. For SEM and EDS, the samples were polished with diamond suspension up to 1 μm and then etched with Kalling's 1. Preparation for EBSD included an additional polishing step with a neutral alumina suspension of particle size 0.04 μm. The Scanning Electron Microscope used was a JEOL 6500FD equipped with a Thermo Fisher NSS EDS system. EBSD measurements were done with a step size of 0.1 μm in a FEI Quanta-450 Field Emission Scanning Electron Microscope with a Hiraki-Pro EBSD detector. The software used for data analysis was EDAX-TSL OIM Data Collection 7.

The volume fraction of sub-micrometric and micrometric precipitates was determined according to the ASTM E1245-03 standard [25], using six different secondary electron images per sample and the image analysis software *ImageJ*.

Vickers hardness measurements were made in order to track this mechanical property with the different heat treatments; the load used was 0.3 kgf and nine indentations per sample were made.

2.2.2. Positron Annihilation Spectroscopy Doppler Broadening

The samples in the reference state and annealed states were submitted to Positron Annihilation Spectroscopy Doppler Broadening (PASDB), at the Delft Variable Energy Positron (VEP) beam, Reactor Institute Delft. Positron Annihilation Spectroscopy is a suitable technique to study defects in materials, with high sensitivity to open volume defects like vacancies. Thus, it is a very useful technique to study radiation damage in metals. At the Delft VEP facility, positrons emitted by a ^{22}Na source, after moderation, can be accelerated to energy values that range from 0.1 keV to a maximum of 25 keV and then implanted in a sample, allowing defect analysis at different depths of material, as determined by

$$\langle z \rangle = \frac{A}{\rho} E^{1.62} \quad (1)$$

where A is an empirical constant, ρ is the density of the material, $\langle z \rangle$ is the positron mean penetration depth and E is the positron implantation energy [26,27]. For the ODS Eurofer samples, A was

taken as 4×10^4 nm kg m^{-3}.$keV^{-1.62}$ [26] and ρ as 7800 kg m^{-3} (Fe density).

Thermalized positrons diffuse through the material lattice and ultimately annihilate with an electron resulting in the emission of two γ photons. To satisfy conservation of energy and momentum during the annihilation process, for a positron-electron pair at rest, the two γ photons are emitted in opposite directions each carrying an energy of 511 keV. Since the positrons are thermalized before annihilation, their contribution to the momentum can be neglected in comparison to the momenta of electrons in the material. Hence, annihilation of a positron and an electron will result in γ photons emitted with an angle deviating from collinearity and with energies slightly different from 511 keV. The Doppler-shifted photon energy is given by

$$E_{DB} = m_0c^2 \pm \frac{p_e c}{2} \quad (2)$$

where p_e corresponds to the electron momentum component parallel to the γ emission direction, m_0 is the electron rest mass and c is the velocity of light. In metals, the core electrons have a broader momentum distribution than the conduction electrons and thus give a wider γ energy spread.

PASDB uses high energy resolution Ge detectors (FWHM = 1.2 keV at 511 keV) to measure the γ energy spectrum. Two line-shape parameters *S* (sharpness) and *W* (wing) are used to quantify the Doppler-broadening of the 511 keV photo-peak. The *S*-parameter is given by the ratio of counts in a central region of the spectrum, in relation to the total counts, and the *W*-parameter corresponds to the ratio of counts in the extremities of the spectrum. Fig. 2 shows a schematic of a Doppler-broadening spectrum with the γ -energy ranges defining the *S* and *W* parameters indicated. For the experiments, the *S* and *W* regions were determined, respectively, by the momenta regions of $|p_e| < 3.5 \times 10^{-3}\ m_0c$ and $1.0 \times 10^{-2}\ m_0c < |p_e| < 2.6 \times 10^{-2}\ m_0c$.

In a defect-free material, the positrons will diffuse through the interstices between atoms until they annihilate with an electron, which can either be a conduction electron or a core electron. In a material containing open-volume defects, like vacancies, the positrons will be preferentially trapped in those defects, since the repelling Coulomb force is at a minimum [28]. When trapped in an open-volume defect the positron has a higher probability of annihilating with a conduction electron. Annihilation with conduction electrons leads to smaller shifts in the γ energy and, therefore, in γ energies in the S range. Annihilation with more energetic core electrons results in a larger energy shift and, hence, contribute to the W range.

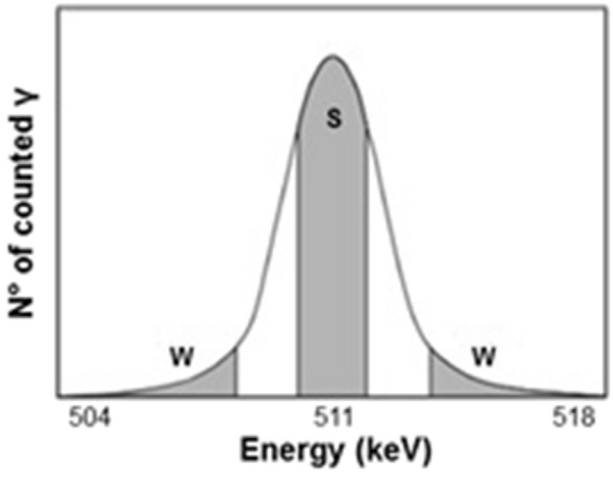

Fig. 2. Schematic of a Doppler Broadening 511 keV annihilation spectrum. The shaded S and W regions are defined such as to obtain maximum sensitivity for annihilations with electrons of low momentum (*S*) or high momentum (*W*).

Samples were prepared for PASDB measurements according to the route summarized in Table 2.

The third step aims to remove the defects introduced in the material during mechanical preparation.

3. Results

3.1. Microstructural characterization

Fig. 3 shows isopleths of the equilibrium diagram calculated with Thermo-Calc for our steel, without the addition of ODS particles. Fig. 3(a) displays a general identification of the microconstituents, including the phases formed in the miscibility gap, while Fig. 3(b) presents all phases that can be formed at a Cr content of 9 wt %, indicated by the vertical line in the diagram. Besides the well-known γ (FCC) and α (BCC), δ is the paramagnetic high-temperature ferrite, $M_{23}C_6$ is a Cr-rich carbide, Laves Phase is a complex intermetallic phase rich in W, σ is an Fe-Cr intermetallic and α' is the BCC Cr-rich phase product of spinodal decomposition. Fig. 4 presents the equilibrium molar fractions of the phases identified in Fig. 3(b) as a function of temperature, where δ-ferrite is considered as α.

Despite their appearance in the equilibrium diagrams, we do not expect to find α' and Laves Phase in the microstructure of the ODS Eurofer steel. The Laves Phase in 9–12% Cr steels is a microconstituent with hexagonal structure and a general composition of $(Fe, Cr)_2(W, Mo)$ [29], however, its precipitation is very slow. The Laves Phase appears only after long time exposure to temperatures up to 650 °*C* (around 900 K) playing, then, a detrimental role in the creep resistance of steels [29–31]. The spinodal decomposition that produces nanoclusters of α and α' is a very slow process in 9–12% Cr steels and typically takes hundreds of hours of exposure to intermediate temperatures to occur [32].

The microstructure of the steel in the different annealing conditions was characterized by SEM, EDS and EBSD. Shape and chemical composition of carbides were obtained with SEM and EDS, while analysis of the matrix was obtained with EBSD. Observation of Y-O based nanoclusters was not possible with any of the mentioned techniques due to their nanometric dimensions (diameter in the range of 4–20 nm). The observation of ferrite/martensite grain boundaries was not clear with SEM, while with EBSD it was not possible to obtain information about the precipitates ($M_{23}C_6$ carbides, according to ThermoCalc).

Fig. 5 shows a secondary electron micrograph of the sample annealed at 600 K, in which it is possible to see the carbide precipitates distributed in the matrix. The precipitates correspond to the brighter particles with an approximately spherical shape and diameter varying from 40 nm to 500 nm; some of them are indicated by red arrows. The micrograph shows that the grain boundaries in the matrix cannot be well distinguished with the SEM after etching.

The microstructures of samples in the reference state and annealed at 600 K, 800 K and 1000 K are very similar. In all samples, the precipitates have the same morphology, size distribution and dispersion in the matrix, as seen in Fig. 5. The volume fraction of precipitates under these conditions is given in Table 3. After annealing at 1200 K, 1400 K and 1600 K the carbides are dissolved.

The experimentally determined volume fractions of precipitates (approximately 4%, Table 3) are in agreement with the molar fraction of $M_{23}C_6$ carbides predicted by Thermo-Calc (Fig. 4). The volume fraction of precipitates is low, which agrees with the 0.1 wt % C content in the steel (Table 1), and is approximately constant up to 1000 K.

Table 2
Route used to prepare samples for PASDB measurements.

Step	Description
1. Grinding	SiC paper of different grids: 800, 1200 and 2000 meshes (SiC particle size of 10 μm)
2. Mechanical Polishing	Diamond suspensions with particle size of 3 and 1 μm; neutral alumina suspension with particle size of 0.04 μm
3. Electrolytic etching	Solution of 1% aqueous oxalic acid; 4 V, 0.1 A, 9 min

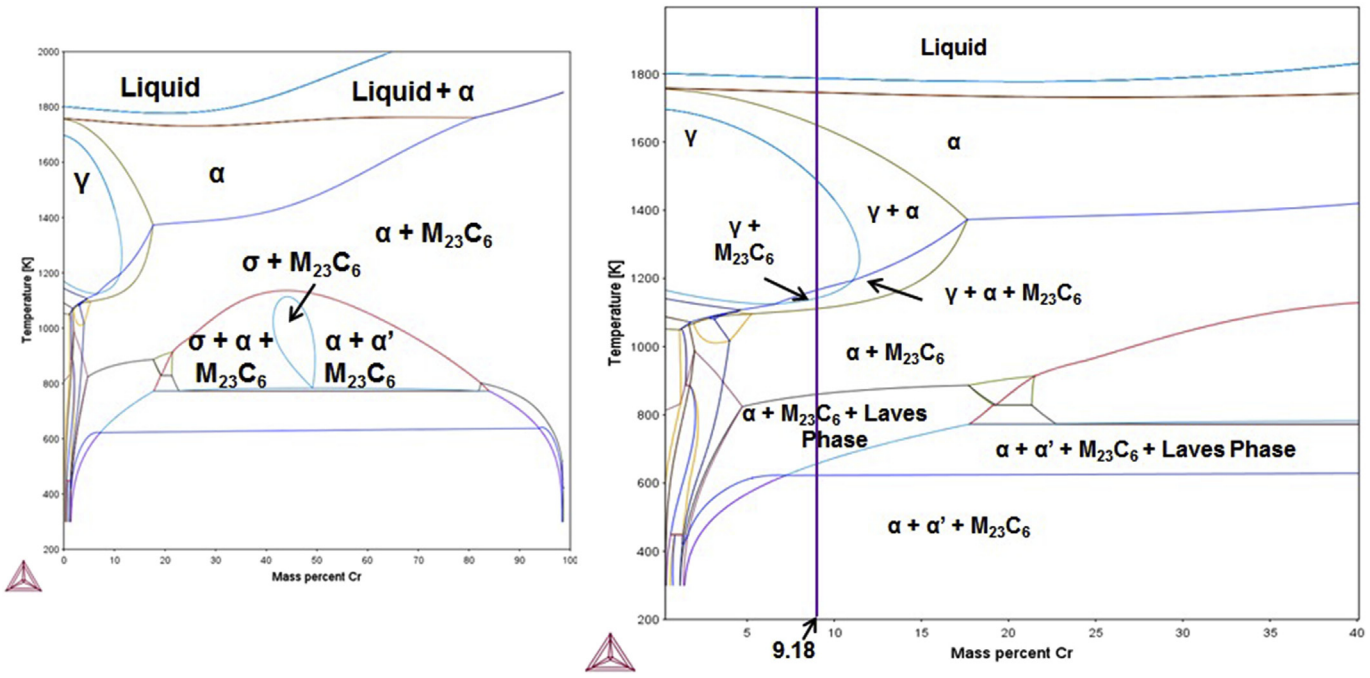

Fig. 3. Isopleths of the equilibrium diagram calculated with Thermo-Calc for the steel without the addition of ODS particles. In (a) the complete equilibrium diagram and in (b) a more detailed view showing the microconstituents formed with a Cr content of 9.18%. Composition used in Thermo-Calc: Fe-0.1C-9.18Cr-1.07W-0.196V; database selected TCFE9: Steels/Fe-alloys v9.0.

According to the Thermo-Calc estimations, the precipitates seen in the microstructure are $M_{23}C_6$. To confirm this, EDS analysis was performed on several precipitates of the ODS Eurofer steel and two distinct composition trends were found: one in which the precipitates have Cr contents higher than 20%, named as P1, and another with Cr content between 10% and 20%, named P2. Table 4 presents the average composition of the precipitates (main metallic elements only) and the Thermo-Calc estimation for the composition of the $M_{23}C_6$ carbide.

The first information we can obtain from Table 4 is that the composition measured with EDS is quite different from the Thermo-Calc estimations. The second information relates to the presence of V in the precipitates P1 and P2: V was indeed detected in some of them, but the error associated with the average value was high. The morphology and contrast of precipitates P1 and P2 are the same. The observations indicate that P1 and P2 precipitates are $M_{23}C_6$, but the size of the precipitates in relation to the interaction volume of the electron beam influences the values measured. All EDS measurements were made with an acceleration voltage of 10 keV, which results in an interaction depth of 500 nm (Kanaya-Okayama range) [33]. This interaction depth is larger than the diameter of most carbides observed in the steel, which results in a simultaneous signal from the matrix, leading to the higher Fe contents and higher Cr/W ratio displayed in Table 4. Precipitates containing Ta were not encountered in any of the SEM/EDS analysis, reflecting the low Ta content added to the steel (Table 1).

Fig. 6 shows the dilatometry results for the 0.3% Y_2O_3-ODS Eurofer steel studied. The A_{c1} and A_{c3} temperatures correspond to the points of deviation from linear thermal expansion, and are, respectively, 1152 K and 1187 K. The values are in good agreement with the literature [13,20,22].

Upon heating, A_{c1} corresponds to the temperature at which the $\alpha \rightarrow \gamma$ transformation starts. At A_{c3} the transformation finishes, and this leads to a fully austenitic microstructure in a non-ODS ferritic/martensitic steel. However, there is experimental evidence that in ODS steels the ferrite does not transform completely into austenite, due to the pinning of α/γ interfaces by Y-O based nanoparticles [20]. Upon cooling, we can see a deviation from linearity at 674 K (indicated as M_s in Fig. 6) that marks the transformation of austenite into martensite. By switching off the power of the dilatometer, between 1573 and 674 K, the average cooling rate obtained was 4.6 K s^{-1}, high enough to form martensite in ODS 9 Cr steels [34]. According to Ukai et al. [34], ODS 9 Cr steels require critical cooling rates in the order of hundreds of K.h^{-1} (100 K h^{-1} = 0.03 K s^{-1}) to form martensite, while non-ODS 9 Cr steels need cooling rates of approximately 20 K h^{-1} They attributed the loss in quenchability of ODS 9 Cr steels to the presence of oxide nanoparticles [34]. During austenitization, the oxide particles pin the austenite grain boundaries and hinder austenite grain growth. During cooling, laths of martensite do not have space to grow within nanosized prior-austenite grains [34]. The dilatometer curves show that martensite has formed in the 0.3% Y_2O_3-ODS Eurofer steel, but the morphology is found to be different from laths.

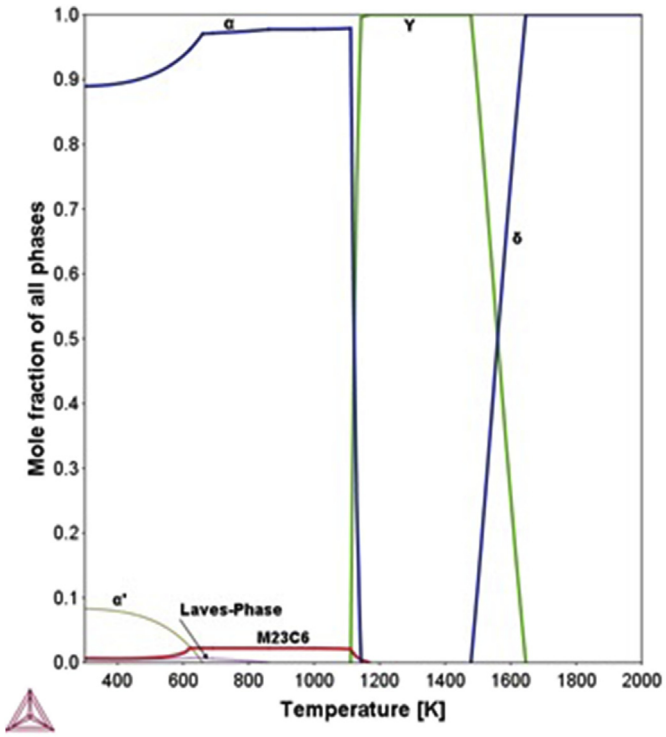

Fig. 4. Molar fraction of phases formed in equilibrium, calculated with Thermo-Calc for the ODS Eurofer steel. Composition used in Thermo-Calc: Fe-0.1C-9.18Cr-1.07W-0.196V.

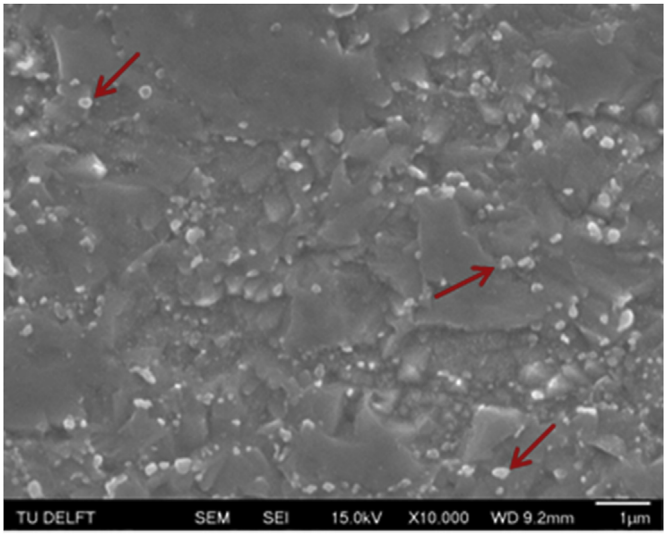

Fig. 5. Secondary electron micrograph of ODS Eurofer after annealing at 600 K. Etchant: Kallings 1.

Table 3
Volume fraction of precipitates calculated for the reference state sample and the samples annealed at 600 K, 800 K and 1000 K.

Sample	Precipitate volume fraction (% ± standard deviation)
Reference	3.2 ± 0.6
600 K	4.5 ± 0.8
800 K	3.2 ± 0.2
1000 K	3.7 ± 1.0

Table 4
Average chemical composition of precipitates present in the ODS Eurofer steel in the reference state and after annealing at 600 K, 800 K and 1000 K, measured with EDS. For comparison with experimental data, Thermo-Calc estimated composition of the $M_{23}C_6$ carbide.

Type of precipitate	Average weight% ± standard deviation of main elements			
	Cr	Fe	W	V
$M_{23}C_6$ – ThermoCalc composition	55	21	16	3
P1	28 ± 6	64 ± 9	4 ± 2	Detected
P2	15 ± 3	79 ± 6	2 ± 1	Detected

Fig. 7 shows the orientation image maps of the samples, as obtained by EBSD, which allow the observation of the matrix microstructure of the ODS Eurofer steel. The colour coded map presented is the Inverse Pole Figure (IPF) for ferrite.

The microstructures in the reference state and after annealing at 600 K, 800 K and 1000 K are essentially the same. The matrix is formed by micrometric grains (average size varying from a few μm to tens of μm), surrounded by smaller grains, with average size in the order of hundreds of nanometers. This heterogeneous microstructure is characteristic of ODS steels produced by mechanical alloying [10,12,13,15,19,20]. The large grains are likely retained ferrite that has undergone grain growth while the smaller grains correspond to tempered martensite. As a reminder, these samples also contain $M_{23}C_6$ carbides that were not indexed in the EBSD analysis, but were observed with SEM. The reference state corresponds to a tempered state (austenitization at 1253 K, quenching and tempering at 1033 K for 1.5 h), and annealing at temperatures below the transition to austenite is an extra tempering stage. Within the large grains, an orientation gradient can be noticed, which indicates that the material has not recovered completely from the severe deformation caused by mechanical alloying. The samples in the reference state and annealed at 600 K still retained the grain elongation caused by hot rolling, which is more evident in the micrometric grains. The arrows in Fig. 7(a) and (b) indicate the working direction and appear different from each other due to positioning inside the microscope, both were cut from the top surface of the original plate. The grain elongation is not visible after annealing above 800 K.

According to Figs. 3 and 6, at 1200 K the material is going through austenitization and, upon cooling, fresh non-lath martensite should form. The approximate cooling rate obtained by switching-off the furnace after this treatment was of 0.5 K s^{-1}, higher than the critical cooling rate for martensite formation of 0.03 K s^{-1} determined by Ukai et al. [34]. Therefore, the observed nanometric grains are fresh non-lath martensite and the micrometric grains correspond to retained ferrite. The $M_{23}C_6$ carbides dissolve during annealing at 1200 K and do not re-precipitate upon cooling, further indicating that, indeed, the final microstructure contains fresh martensite enriched in C. The microstructure of the steel after annealing at 1200 K keeps the degree of refinement seen in the previous conditions, confirming the role of the Y-O based nanoparticles in hindering grain boundary movement.

According to the equilibrium phase diagram (Fig. 3), at 1400 K the material is in the austenitic field and a microstructure similar to Fig. 7(e) was expected. Surprisingly, Fig. 7(f and h) shows a smaller volume fraction of nanometric non-lath martensite and a higher volume fraction of micrometric grains. Also, it is observed that some of the micrometric grains no longer contain orientation gradients, which indicates the loss of their intrinsic deformation, likely due to recrystallization. The observed grain coarsening suggests that in some regions of the material the oxide nanoparticles did not fully prevent grain growth. This odd aspect is discussed in Section 4.

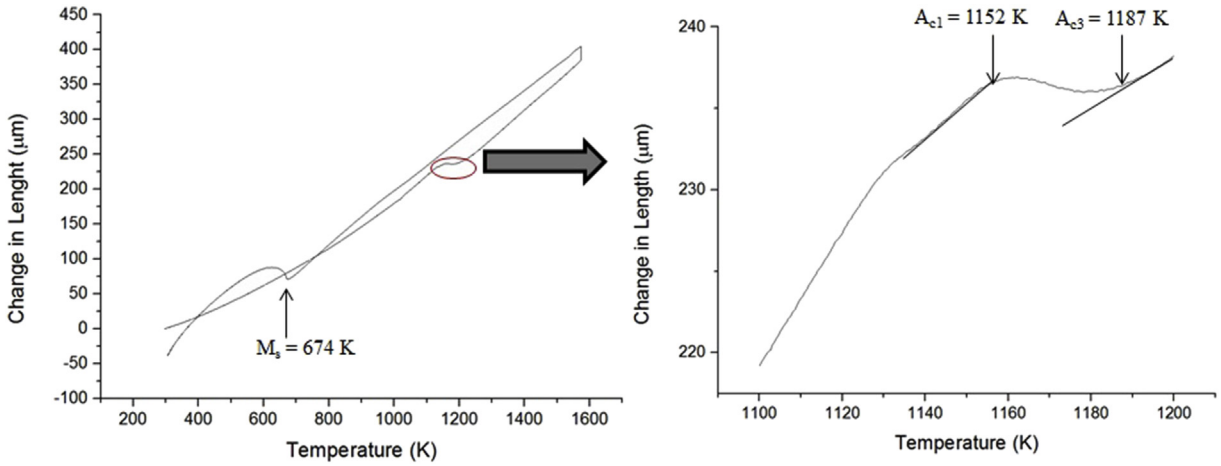

Fig. 6. Dilatometry curve obtained for the ODS Eurofer steel with a heating rate of 1 K s^{-1}, until 1573 K. After holding for 5 min at the maximum temperature, the sample was cooled, at an average rate of 0.8 K s^{-1}, by switching-off the HF power system of the dilatometer.

After annealing at 1600 K a coarser, deformation-free microstructure is formed (Fig. 7(i)), indicating the continuation of the processes started at 1400 K. Also, at 1600 K the material is in the γ+δ field (Fig. 3) and the Image Quality maps in Fig. 7(i1-i2), obtained at different areas of the same sample, show islands of martensite among the recrystallized δ-ferrite, which are not clear in the IPF maps. By highlighting the grains with Grain Average Image Quality higher than 50000, it was possible to estimate a volume fraction of δ-ferrite of 58% and, consequently, of 42% of martensite. Laths of martensite can be seen in regions of the sample where prior austenite grains had grown (Fig. 7(i1)).

The Inverse Pole Figure maps presented in Fig. 7 show an effect of the annealing treatments performed on the dominant surface orientation of the samples (DSO). Samples in the reference state and annealed at 600 K and 800 K preserved the DSO induced by hot working of the material. On the other hand, annealing at 1000 K was enough to alter the hot-deformation DSO, resulting in the absence of a preferred grain orientation. The same aleatory DSO is observed in samples annealed at 1200 K and 1600 K. However, the origin of the DSO seen at 1400 K (Fig. 7(f)) is unclear.

Fig. 8 shows the grain size distributions obtained with EBSD for each sample and Fig. 9 the Vickers Hardness results. The grain size distributions follow a lognormal behaviour. In the reference state and after annealing between 600 and 1000 K, the grain size distributions are statistically very similar and this is reflected in the constant Vickers hardness. Nevertheless, the insert in Fig. 8 containing the zoomed-in of these distributions shows a slight shift towards larger grain sizes for the annealed samples in relation to the reference state, suggesting that sub-grain growth occurs to some extent. In terms of grain size, the sample treated at 1200 K has a behaviour similar to the previous ones, however its Vickers hardness is the highest. This peak in Vickers hardness can be attributed to the formation of fresh equiaxed-martensite and to grain refinement strengthening. The carbon and metallic alloying elements that were previously forming $M_{23}C_6$ carbides are redistributed in the matrix in the form of solid solution or segregated at dislocations and grain boundaries, present in high densities in ODS steels due to mechanical alloying. Therefore, strengthening by solid solution or segregation of alloying elements contribute for the hardness peak measured.

After annealing at 1400 K, the Vickers hardness has a value similar to that of the reference state and the samples annealed at 600–1000 K. Although its grain size distribution is the most heterogeneous, we can still see a considerable fraction of fine grains with diameter between 1.5 and 4 μm that contribute to the strengthening of the steel (Fig. 7(h)). We can understand this hardness value by the combination of four factors: presence of martensite, solid solution strengthening, dispersion of Y-O based nanoparticles and a fine grain structure. Finally, we observe a drastic decrease in hardness after annealing at 1600 K, which agrees with the overall coarsening of the microstructure.

3.2. Positron Annihilation Spectroscopy Doppler Broadening

The 0.3% Y_2O_3-ODS Eurofer steel has a high concentration of defects that are intrinsic to the microstructure, like grain boundaries, interfaces of $M_{23}C_6$ precipitates, dislocations, interfaces of Y-O based nanoparticles and solute elements. With the exception of oxide nanoparticles, these defects would also be present in a non-ODS Eurofer steel. The 0.3% Y_2O_3-ODS Eurofer steel was fabricated by mechanical alloying, a process that subjects the material to severe deformation. Even after consolidation and heat treatment, a considerable fraction of defects caused by deformation remains stored in the microstructure in the form of a high grain boundary surface area, as we could see in Fig. 7. We have also observed, in the Inverse Pole Figure OIM maps of Fig. 7, an orientation gradient inside many grains for almost all annealed samples, confirming the existence of a deformation state in the material. Therefore, in addition to the cited defects intrinsic to the microstructure the 0.3% Y_2O_3-ODS Eurofer steel also contains defects introduced during mechanical alloying. We will refer to this type of defects as carriers of deformation. Then, to interpret the PASDB results we will take into account the defects intrinsic to the microstructure, the Y-O based nanoparticles and the carriers of deformation.

Fig. 10 shows the *S*-parameter and *W*-parameter as a function of the positron implantation energy and positron implantation depth (top axis). Average values for *S* and *W* were calculated for each annealing condition using the data obtained at implantation energies above 10 keV, which are representative of events occurring in the bulk. The obtained S_{bulk} and W_{bulk} values are plotted in Fig. 11 as a function of the annealing temperature. Fig. 12 displays the *SW* map of the steel, which was obtained by plotting W_{bulk} of each condition *vs* its respective S_{bulk}. Note that high *S* (low *W*) values are related to a high concentration of defects in the material. By definition an in(de)crease of *S* is accompanied by a de(in)crease in *W*. When only two types of non-altering positron traps are involved, the slope of the line connecting (S,W) points, given by the ratio R =

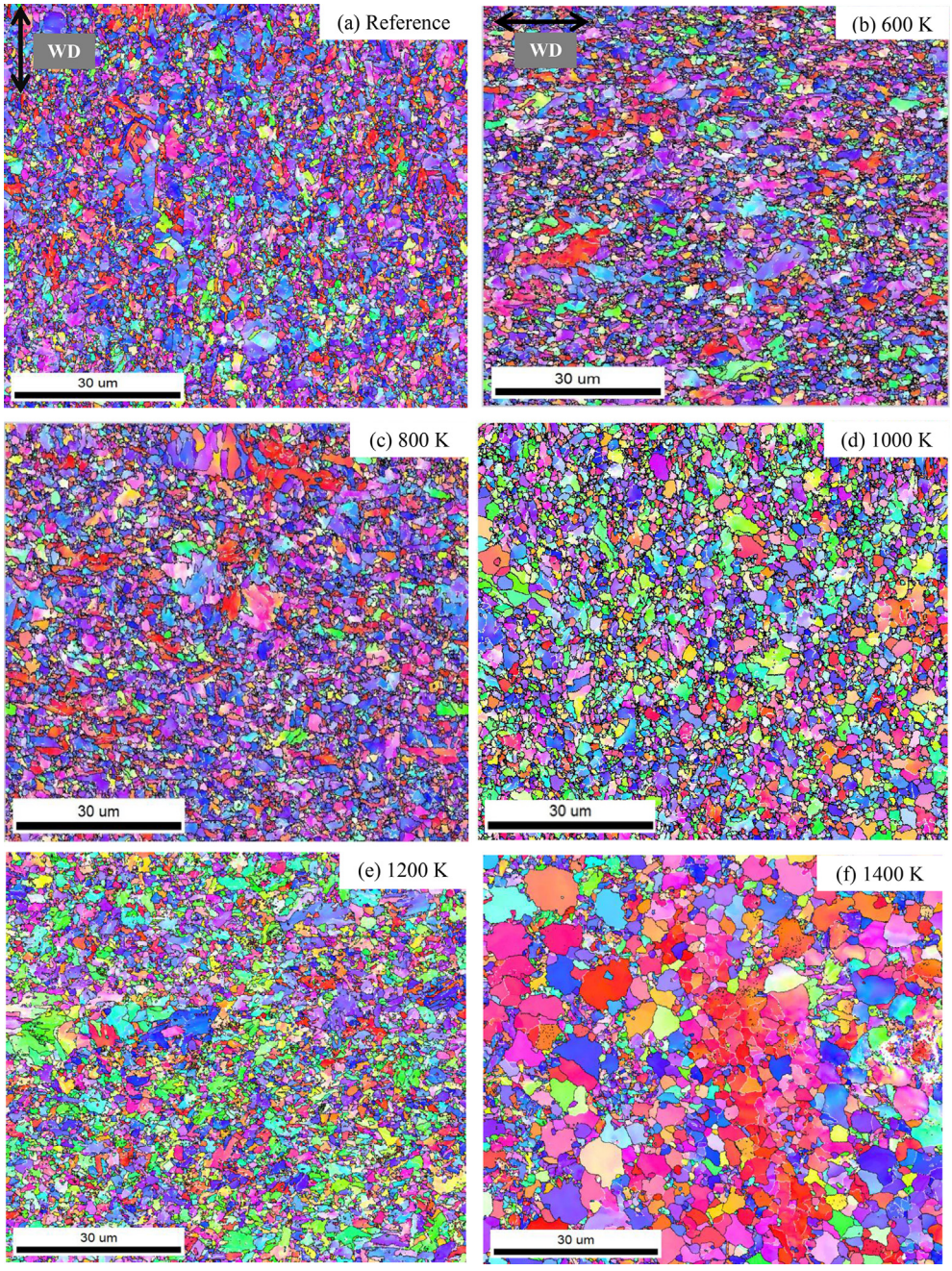

Fig. 7. Orientation image maps obtained for ODS Eurofer steel after annealing at the temperatures indicated for 1 h. Colour coded map: inverse pole figure for ferrite, Grayscale maps: image quality of samples annealed at (g) 1200 K, (h) 1400 K and (i1, i2) of regions of the sample annealed at 1600 K, containing martensite (darker grains). (For interpretation of the references to colour in this figure legend, the reader is referred to the Web version of this article.)

$\left|\frac{\Delta S}{\Delta W}\right|$, should be constant. A change in slope thus indicates (additional) positron trapping at a different type of defect. If this change in slope is ascribed to the *W*, which derives from annihilations with core electrons, it may indicate a different chemical environment at the positron trapping/annihilation site [28,35].

For treatments up to 1200 K, a continuous decrease in *S* and increase in *W* with annealing temperature is seen, which is indicative of a decrease in defect concentration. Then, after annealing at 1400 K and 1600 K, the *S*-parameter increases strongly, reaching values higher than in the reference state. The opposite behaviour is seen for *W*. The location of the two latter states in the *SW* map shows that the nature of those defects is different from the ones detected in the reference state and in the samples annealed at lower temperatures.

Fig. 13 shows the equilibrium density of thermal vacancies in ferrite and austenite *vs* temperature. The equilibrium density of thermal vacancies was calculated according to:

$$C_{th.\ vac.} = N_{Fe}\exp\left(\frac{-E_f}{kT}\right) \quad (3)$$

where N_{Fe} is the Fe atomic density (8.47×10^{28} m^{-3}), E_f is the

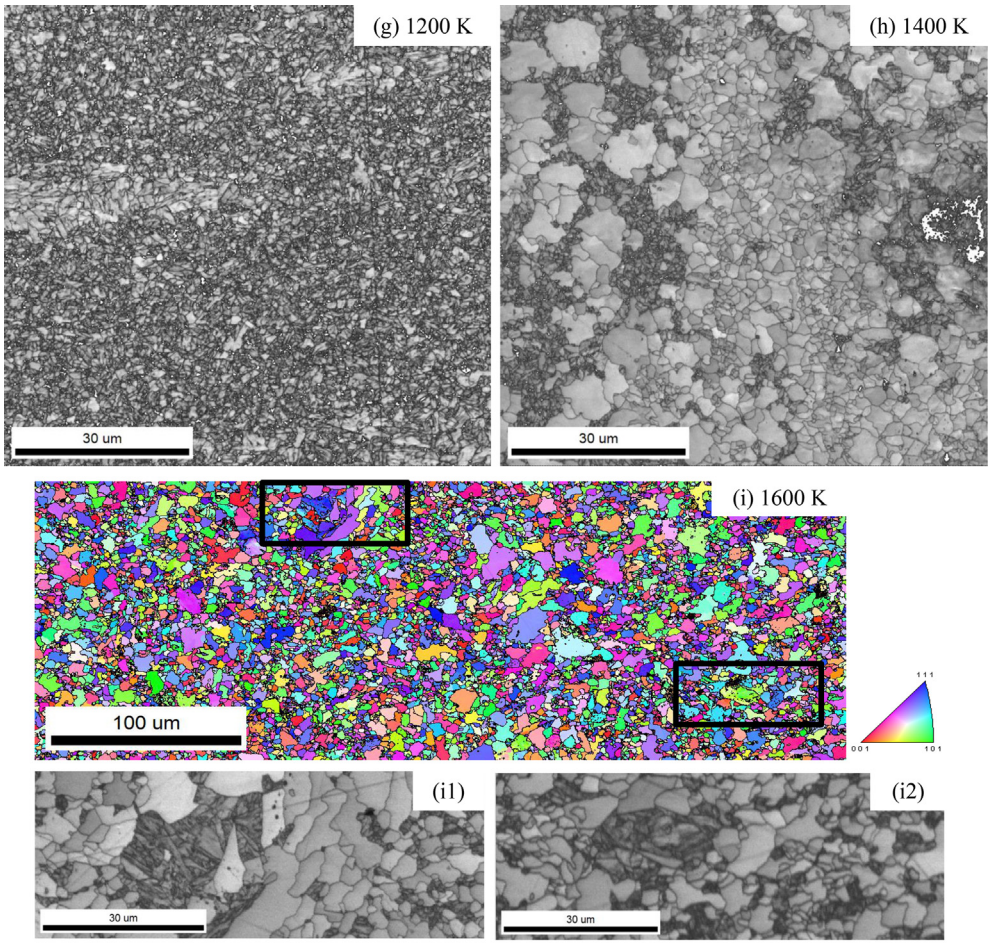

Fig. 7. (*continued*).

vacancy formation energy in the metal, k is the Boltzmann constant and T is the temperature. For ferrite, we used $E_f = 1.6$ eV [36] and for austenite, $E_f = 1.4$ eV [36]. In this estimated quantification, we consider only the contribution of Fe vacancies and we do not take into account the effect of Cr, or other alloying elements, on the vacancy formation energy [37].

In Fig. 13, when the material is above 1200 K, the equilibrium density of thermal vacancies in ferrite and austenite increases significantly, being 2 to 4 orders of magnitude higher than in ferrite at 1000 K. The density of thermal vacancies in ferrite at 1200 K and above is considered because it coexists with austenite in the material, due to the incomplete austenitization of ODS 9 Cr steels (1200 K–1400 K) [13,20] and to the entrance in the dual phase field $\gamma+\delta$ at 1600 K (Fig. 3). At 1400 K and 1600 K, besides the higher density of thermal vacancies, the Fe atoms also present an increased self-diffusivity, especially in ferrite [38–40] and, consequently, the thermal vacancies are more mobile. These characteristics of Fe can explain the *SW* behaviour observed at 1400 K and 1600 K. The hypothesis is that the Y-O based nanoparticles in the steel are trapping and stabilizing thermal vacancies at all annealing temperatures. Nevertheless, at 1400 K and 1600 K, the higher density of thermal vacancies, with increased mobility, form larger clusters that are trapped to the Y-O nanoparticles. Upon cooling, the larger vacancy clusters stay in the microstructure, leading, then, to the high *S* values and change in trend for the *SW* pairs seen in Fig. 12.

A similar annealing study was previously carried out for the non-ODS Eurofer steel [41]. In the non-ODS steel only a continuous decrease in *S* and increase in *W* with annealing up to 1600 K was observed (Fig. 14) [41]. Thermal vacancies were also formed in the non-ODS Eurofer steel, however, because Y-O based clusters are not present, the thermal vacancies are not retained in the structure upon cooling. The trend observed in Fig. 14 for the non-ODS Eurofer steel was associated with a general decrease in defect concentration due to events like tempering of martensite, grain growth, dissolution of carbides and martensite formation after annealing at 1200, 1400 and 1600 K [41].

A consideration of all microstructural changes occurring in the non-ODS Eurofer steel was necessary to understand the defect evolution detected with positrons. For the 0.3% Y_2O_3-ODS Eurofer steel this type of analysis is even more complex, since the whole microstructure forms and evolves differently due to the Y-O based nanoclusters. In addition, the steel contains another class of defects, the carriers of deformation described earlier, which are responsible for the overall higher *S* and lower *W* depicted in Fig. 14. In section 4 we discuss the PASDB results in relation to these factors.

4. Discussion

4.1. Analysis of material in the reference state and annealed at 600 K, 800 K and 1000 K

The microstructural observations made with SEM and EBSD in Section 3.1 show that annealing at 600 K, 800 K or 1000 K does not

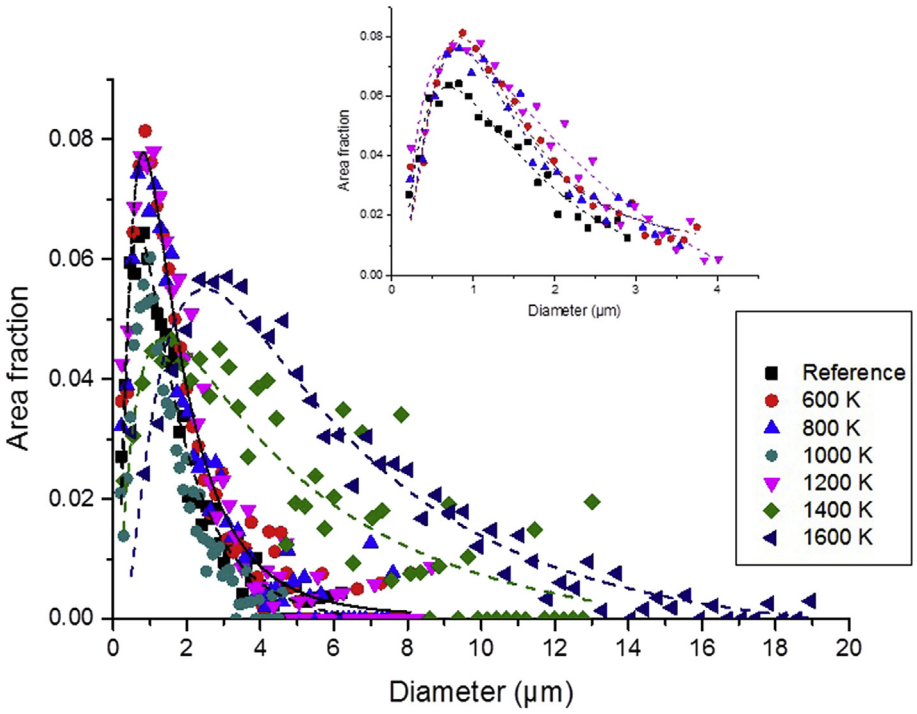

Fig. 8. Grain size distribution obtained for samples in the reference state and after annealing at 600 K, 800 K, 1200 K, 1400 K and 1600 K. Insert: detailed view of encircled peaks of the reference state, 600 K, 800 K and 1200 K samples.

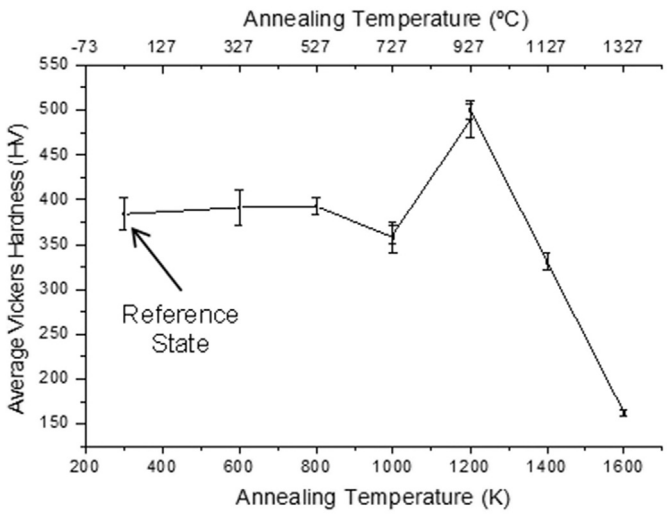

Fig. 9. Vickers hardness values measured for ODS Eurofer in the reference state and after annealing for 1 h at different temperatures.

alter the reference state microstructure significantly, except for the grain size distribution shifting towards higher grain sizes (Table 3, Fig. 7(a–d) and Fig. 9). Additionally, these annealing treatments do not have an effect on the average Vickers hardness of the material (Fig. 10). On the other hand, the PASDB results presented in Section 3.2 show (1) a continuous decrease in defect concentration with annealing up to 1000 K and (2) the *SW* pairs in Fig. 12 vary linearly, suggesting the removal of a type of defect that is common to all these conditions. Based on these observations, it is possible to conclude that the only microstructural process occurring with annealing between 600 and 1000 K is the recovery of the deformed state of the material, introduced during mechanical alloying. Hence, the decrease in the concentration of defects and the linear variation of *SW* is mainly due to the removal of carriers of deformation.

4.2. Analysis of material annealed at 1200 K

After annealing at 1200 K, the Vickers hardness reaches a maximum value, indicating that, upon cooling, the martensitic transformation occurs. A first expectation would be of the increase in defect concentration, mainly of martensite grain boundaries, dislocations and vacancies associated with this constituent, but the PASDB results show exactly the opposite: the concentration of defects is the lowest after this heat treatment. To better understand this conflicting behaviour, we need to analyse separately the evolution of defects intrinsic to the microstructure (carbide interfaces, grain boundaries, dislocations associated to martensitic transformation) and of the carriers of deformation (defects introduced during mechanical alloying). At 1200 K, $M_{23}C_6$ carbides are dissolved and, upon cooling to room temperature, do not re-precipitate. Equiaxed martensite is formed, along with new dislocations. In comparison to samples in the reference state and annealed between 600 and 1000 K, the average grain size of the equiaxed martensite does not change significantly and, therefore, neither does its contribution to *S* and *W* values (the grain boundary surface area of martensite remains constant). The creation of dislocations in the martensitic transformation is balanced by the removal of carbide interfaces, in terms of the contributions to positron annihilation. This proposed balance of defects intrinsic to the microstructure agrees with the results obtained previously for the non-ODS Eurofer steel, which does not present the high deformation state seen in the ODS material [41]. Fig. 14 shows that the *S* and *W* values of the non-ODS Eurofer annealed at 1000 K and 1200 K are the same: tempering of martensite, grain growth and interfaces of $M_{23}C_6$ carbides at 1000 K are in balance with $M_{23}C_6$ dissolution and creation of new defects due to martensite

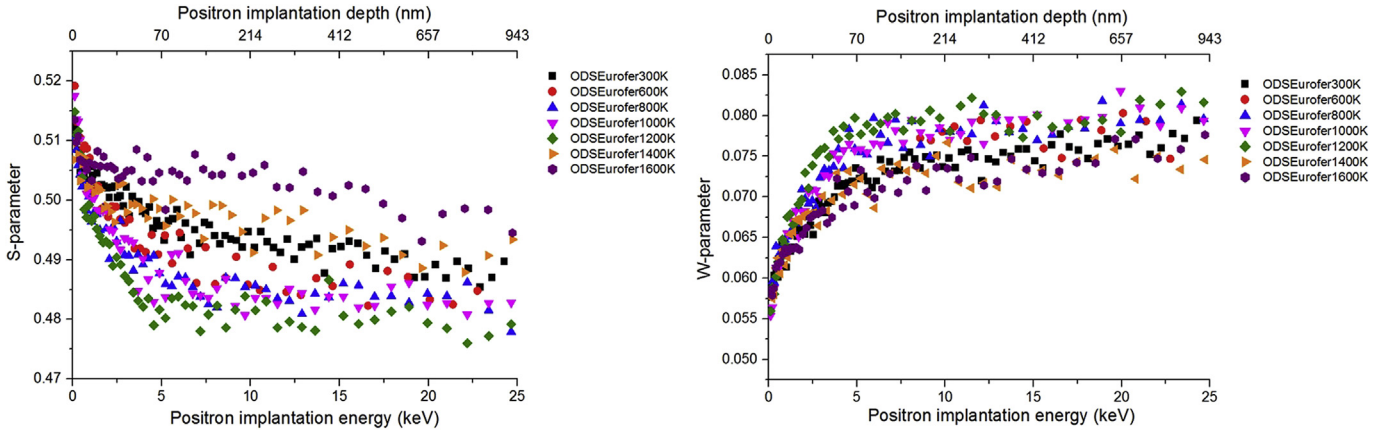

Fig. 10. *S*-parameter and *W*-parameter as a function of positron implantation energy and positron implantation depth.

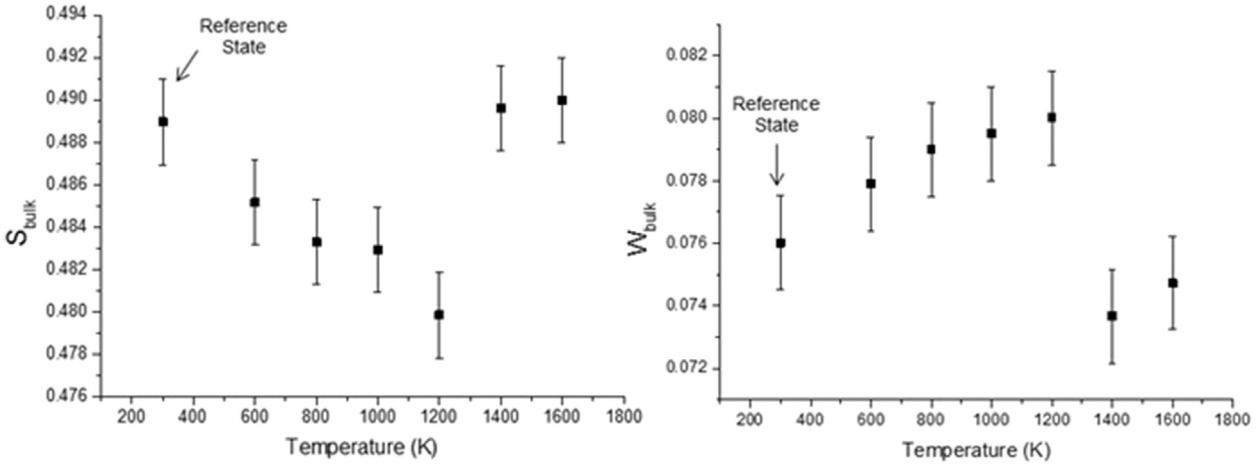

Fig. 11. S_{bulk} and $W_{bulk,}$ calculated as the average of the data obtained with positron energies above 10 keV, *vs* the annealing temperature.

formation upon cooling from 1200 K. It is important to mention that the non-ODS Eurofer was cooled under the same cooling rate as the 0.3% Y_2O_3-ODS Eurofer, an average of 0.5 K s^{-1}, sufficiently fast to form martensite in both steels (see Fig. 7(g)). Perhaps the use of a higher cooling rate would lead to the substantial increase in defect concentration in the non-ODS Eurofer steel. As mentioned earlier, the 0.3% Y_2O_3-ODS Eurofer steel has extra categories of defects: oxide nanoparticles and the carriers of deformation. Up to 1200 K we do not observe any microstructural instability in the material, indicating that no changes are occurring with the Y-O based nanoparticles present in the material and, therefore, their contribution to *S* and *W* values can be considered constant as well. Hence, the further decrease in *S* observed after annealing at 1200 K is likely due to the continuous removal of carriers of deformation, which we can think of as a surplus of dislocations present in ODS steels. In Fig. 14, the position of the *SW* pair of the sample annealed at 1200 K follows the same slope as the previous samples (reference state and annealed at 600–1000 K), confirming that the nature of detected defects is the same. Sallez et al. [12] measured with *in-situ* XRD the dislocation density in an ODS ferritic steel, during annealing at 900 °C (1173 K) for 3000 s. The dislocation density measured was of 3.5 × 10^{15} m^{-2}, at least two orders of magnitude higher than in a non-ODS steel [12]. This supports our PASDB observations and our hypothesis.

It is interesting to point out how SEM, EBSD, Vickers hardness and PASDB complement each other in the analysis of microstructural and defect evolution with annealing at temperatures between 600 K and 1200 K. The first three techniques characterize the structural features related to phase transformations (dissolution of $M_{23}C_6$ carbides and martensitic transformation) and PASDB allows the understanding of the evolution of the deformation state in the material.

4.3. Analysis of material annealed at 1400 K and 1600 K

After annealing at 1400 K and 1600 K, the results obtained with SEM, EBSD and Vickers hardness indicate that the Y-O based nanoparticles lose their function of maintaining the microstructure thermally and mechanically stable. However, these techniques cannot give information about the mechanism behind this loss of functionality, whether if it is due to dissolution of the nanoparticles or due to their coarsening. Other authors [13,42] observed, with Transmission Electron Microscopy, the coarsening of Y-O based nanoparticles, after annealing at 1300–1350 °C (1573–1623 K), in different ODS steels. Additionally, the PASDB results shown in Figs. 10–12 suggest that the oxide nanoparticles are present in the matrix at 1400 K and 1600 K, trapping and stabilizing thermal-vacancy clusters. If the particles were dissolved, the thermal vacancies would be annealed out of the material during cooling inside the furnace, and the *SW* behaviour would be similar to the non-ODS

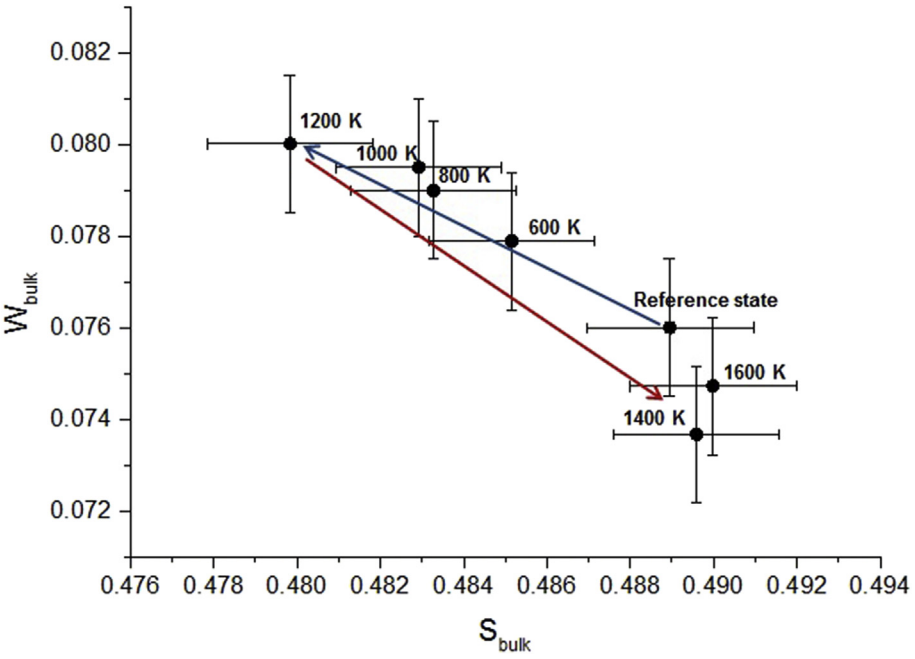

Fig. 12. *SW* map of the 0.3% Y_2O_3-ODS Eurofer steel. The blue arrow indicates the evolution of the *SW* pair from the reference state until annealing at 1200 K. The red arrow shows the change in behavior after annealing at 1400 K. The *SW* location after annealing at 1400 and 1600 K suggests that positrons detect a type of defect different from the previous conditions. (For interpretation of the references to colour in this figure legend, the reader is referred to the Web version of this article.)

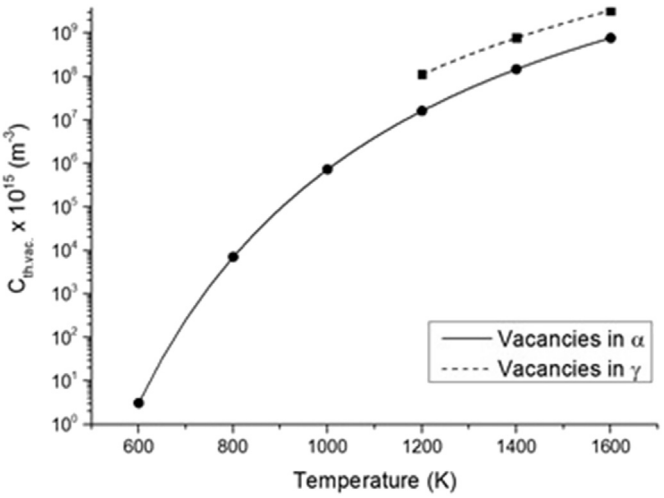

Fig. 13. Equilibrium density of thermal vacancies in ferrite and austenite *vs* annealing temperature.

Eurofer steel [41], presented in Fig. 14. Still, a proper characterization of the oxide nanoparticles with Transmission Electron Microscopy (TEM) and Atom Probe Tomography (APT) is necessary to confirm their coarsening, especially at 1400 K.

The results obtained by Ortega et al. [23] further support the hypothesis of Y-O based nanoparticles trapping thermal vacancies. The authors [23] have assessed the effect of annealing treatments on as-consolidated Y_2O_3-ODS Eurofer, using Positron Annihilation Lifetime Spectroscopy (PALS) and TEM [23]. After annealing at 1523 K, the authors observed an increase in positron lifetime, which they attributed to the stabilization of Ar-vacancy clusters by Y-O based nanoparticles. TEM images of their material, after annealing at 1523 K, show Ar-vacancy voids located at the interfaces of the Y-O based particles [23]. Residual Ar contents can be introduced in ODS steels during mechanical alloying, since the process is normally performed under Ar atmosphere. However, given that our steel was heat treated several times after consolidation, we consider that all possible residual Ar in solid solution was partially annealed out of the material and partially trapped at oxide nanoparticles interfaces. Therefore, the contribution of possible Ar atoms-vacancy clusters stabilized by oxide nanoparticles is accounted in our *S* and *W* values for all samples. When further annealed at 1400 K and 1600 K, extra thermal vacancies are formed and trapped in the material, becoming the main contributors for *S* and *W* in these conditions.

Furthermore, it is important to point out the role of vacancy mobility in our interpretation of the PASDB results. Fig. 13 shows that the density of thermal vacancies at 1200 K is of the same order of magnitude as at 1400 K. Thus, attributing the *SW* behaviour seen at 1400 K and 1600 K solely to the increase in density of thermal vacancies would conflict with the lowest *S* observed after annealing at 1200 K. Fe self-diffusion in austenite at 1200 K is 3 and 4 orders of magnitude lower than at 1400 K and 1600 K, respectively, and 5 orders of magnitude lower than in δ-ferrite at 1600 K [40]. Consequently, at 1200 K, even though the density of vacancies is high, their mobility is still low for the formation of larger clusters.

Finally, a curious aspect to be discussed is the odd microstructure obtained after annealing at 1400 K. The coexistence of regions with nanometric and micrometric grains (Fig. 7(f and h)) indicates that coarsening of oxide nanoparticles has taken place, but not throughout the whole volume of the sample. Hence, in some parts of the sample the main boundary pinning force becomes weaker, allowing grains to grow. At 1400 K the material is in the austenitic field and it is expected that austenite grains subjected to a lower pinning force are able to grow and, upon cooling, form martensite, in lath or block form. Nevertheless, the micrograins seen in Fig. 7(f and h) correspond to recrystallized ferrite. The formation mechanism of this microstructure is not clear yet and more experimental investigations, using *in-situ* X-Ray Diffraction, TEM and APT are necessary to understand it. So far, a possible explanation is that

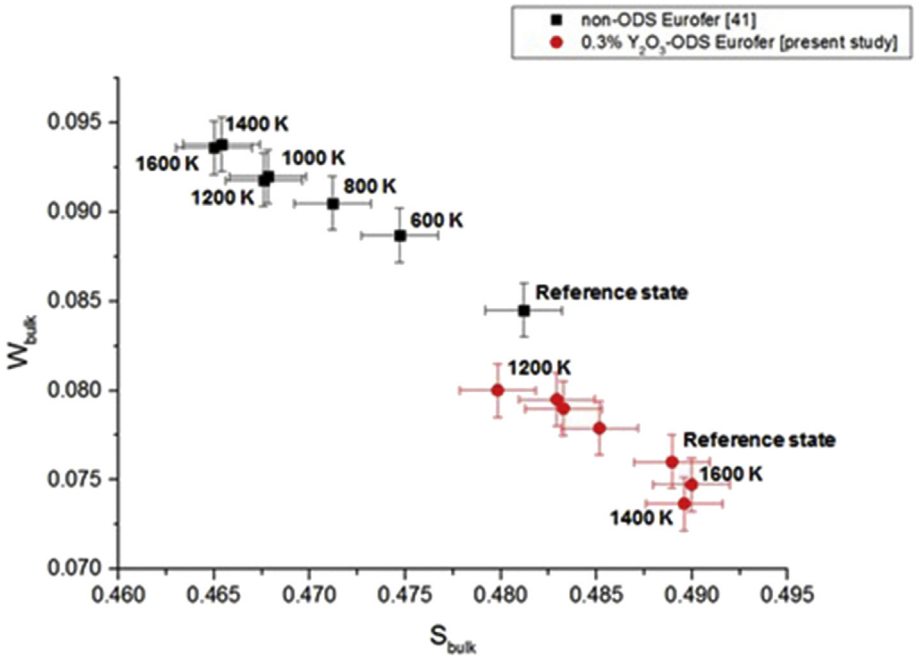

Fig. 14. *SW* map comparing the non-ODS Eurofer steel [41] with the 0.3%-Y_2O_3 ODS Eurofer steel.

recrystallization and growth of retained ferrite is kinetically favoured over austenitization at 1400 K. A first aspect to consider is that the coarsening of oxide nanoparticles, most likely via Ostwald ripening [42], is not an instantaneous process. Hence, during the first minutes of annealing at 1400 K, we can assume that (1) the oxide particles still have their original refined size, (2) incomplete austenitization occurs [20] and (3) the material is formed by austenite and a certain volume fraction of retained ferrite. According to Sandim et al. [42], Y and O diffuse more easily in ferrite than in austenite, at temperatures as high as 1350 °C (1623 K). Again, in our material the oxide nanoparticles lose thermal stability at a lower temperature. Still, it is possible to assume that coarsening of oxide nanoparticles, at 1400 K, occurs preferentially in the regions containing retained ferrite. With the evolution of annealing time, the retained ferrite, subjected to a weaker pinning force and with a high stored deformation energy, goes through continuous recrystallization [12] and the austenite grain boundaries are pinned by the smaller oxide particles. Metals that are severely deformed, like ODS steels, have a high mean grain boundary misorientation, which leads to the occurrence of continuous recrystallization, i.e., growth of deformed grains, without nucleation of new deformation-free ones [21].

5. Conclusions

The characterization of the microstructure and evolution of defects in the 0.3% Y_2O_3 ODS Eurofer steel, after annealing at different temperatures, lead to the following conclusions:

i) The Y-O based nanoparticles and the deformation introduced in the material, during its fabrication by mechanical alloying, strongly influence the microstructure and the kinetics of phase transformations.
ii) The Y-O based nanoparticles are responsible for maintaining the microstructure and the Vickers hardness of the steel stable up to 1000 K.
iii) After annealing at 1200 K, the Vickers hardness of the material markedly increases, due to the formation of martensite. Nevertheless, the microstructure presents the same degree of refinement as in the previous conditions, due to the pinning effect of Y-O based nanoparticles. At 1200 K, the particles prevent the growth of austenitic grains and, upon cooling, nanometric martensite forms.
iv) Regarding the PASDB analysis, annealing up to 1200 K leads to a continuous decrease in the *S*-parameter and increase in the *W*-parameter, suggesting an overall decrease in defect concentration. This *SW* trend is attributed mainly to the recovery of dislocations introduced during mechanical alloying.
v) Annealing at 1400 K leads to the formation of an unexpected dual-phase microstructure, composed of recrystallized ferrite and nanometric martensite. This is a first indication that Y-O nanoparticles are going through coarsening in certain regions of the material. During annealing at 1600 K, coarsening of oxide particles is enhanced and, hence, overall grain growth of δ-ferrite and austenite occurs.
vi) PASDB analysis on the samples annealed at 1400 K and 1600 K show an increase in *S* and a different trend for *SW*. This behaviour is attributed to the formation of thermal-vacancies clusters, which are trapped and stabilized by the Y-O based nanoparticles. Despite not being able to hinder grain boundary movement, the Y-O particles still trap defects like thermal-vacancies.

Data availability

The raw data required to reproduce these findings is available for download.

Credit author statement

Viviam Marques Pereira: conceptualization, methodology,

validation, formal analysis, investigation, resources, data curation, writing – original draft, writing – review and editing.

Henk Schut: term, conceptualization, methodology, validation, formal analysis, investigation, resources, writing – review and editing, supervision.

Jilt Sietsma: term, conceptualization, validation, writing – review and editing, supervision, project administration.

Declaration of competing interest

The authors declare that they have no known competing financial interests or personal relationships that could have appeared to influence the work reported in this paper.

Acknowledgments

This research was carried out under project number T16010e in the framework of the Industrial Partnership Program of the Materials innovation institute M2i (www.m2i.nl) and the Foundation of Fundamental Research on Matter (FOM) (www.fom.nl), which is part of the Netherlands Organisation for Scientific Research (www.nwo.nl).

The authors would like to thank Prof. Roumen Petrov (Ghent University) for the EBSD analysis performed.

References

[1] K.L. Murty, I. Charit, Structural materials for Gen-IV nuclear reactors: challenges and opportunities, J. Nucl. Mater. 383 (2008) 189–195.
[2] R. Lindau, et al., Present development status of EUROFER and ODS-EUROFER for application in blanket concepts, Fusion Eng. Des. 75–79 (2005) 989–996.
[3] S. Ukai, M. Fujiwara, Perspective of ODS alloys application in nuclear environments, J. Nucl. Mater. 307–311 (8) (2002) 749–757.
[4] S. Ukai, et al., Structural Materials for Generation IV Nuclear Reactors, Elsevier, 2017, pp. 357–414 (Chapter 10), Oxide dispersion-strengthened ferritemartensite steels as core materials for Generation IV nuclear reactors.
[5] W.R. Corwin, US Generation IV reactor integrated materials technology program, Nuclear Engineering and Technology 38 (7) (2006) 591–618.
[6] S. Ukai, et al., Tube manufacturing and mechanical properties of oxide dispersion strengthened ferritic steel, J. Nucl. Mater. 204 (1993) 74–80.
[7] R.L. Klueh, J.P. Shingledecker, R.W. Swindeman, D.T. Hoelzer, Oxide dispersion-strengthened steels: a comparison of some commercial and experimental alloys, J. Nucl. Mater. 341 (2005) 103–114.
[8] R.L. Klueh, D.S. Gelles, M. Okada, N.H. Packan, Reduced Activation Materials for Fusion Reactors, ASTM, 1990.
[9] A. Bremaecker, Past research and fabrication conducted at SCK-CEN on ferritic ODS alloys used as cladding for FBR's fuel pins, J. Nucl. Mater. 428 (2012) 13–30.
[10] I. Hilger, et al., Fabrication and characterization of oxide dispersion strengthened (ODS) 14 Cr steels consolidated by means of hot isostatic pressing, hot extrusion and spark plasma sintering, J. Nucl. Mater. 472 (2016) 206–214.
[11] H. Springer, et al., Efficient additive manufacturing production of oxide-and-nitride-dispersion-strengthened materials through atmospheric reactions in liquid metal deposition, Mater. Des. 111 (2016) 60–69.
[12] N. Salez, et al., In situ characterization of microstructural instabilities: recovery, recrystallization and abnormal growth in nanoreinforced steel powder, Acta Materiallia 87 (2015) 377–389.
[13] C. Cayron, E. Rath, I. Chu, S. Launois, Microstructural evolution of Y_2O_3 and $MgAl_2O_4$ ODS Eurofer steels during their elaboration by mechanical alloying and hot isostatic pressing, J. Nucl. Mater. 335 (2004) 83–102.
[14] C. Suryanarayana, Mechanical alloying and milling, Prog. Mater. Sci. 46 (2001) 1–184.
[15] A. Garcia-Junceda, M. Campos, N. Garcia-Rodriguez, J.M. Torralba, On the role of alloy composition and sintering parameters in the bimodal grain size distribution and mechanical properties of ODS ferritic steels, Metall. Mater. Trans. 47 (2016) 5325–5333.
[16] T. Okuda, M. Fujiwara, Dispersion behaviour of oxide particles in mechanically alloyed ODS steel, J. Mater. Sci. Lett. 14 (22) (1995) 1600–1603.
[17] Y. Kimura, S. Takaki, S. Suejima, R. Uemori, H. Tamehiro, Ultra-grain refining and decomposition of oxide during super-heavy deformation in oxide dispersion ferritic stainless steel powder, ISIJ Int. 39 (2) (1999) 176–182.
[18] M. Brocq, et al., Nanoscale characterization and formation mechanism of nanoclusters in an ODS steel elaborated by reactive-inspired ball-milling and annealing, J. Nucl. Mater. 409 (2011) 80–85.
[19] N. Sallez, et al., On ball-milled ODS ferritic steel recrystallization: from as-milled powder particles to consolidated state, J. Mater. Sci. 50 (2015) 2202–2217.
[20] M. Yamamoto, S. Ukai, S. Hayashi, T. Kaito, S. Ohtsuka, Formation of residual ferrite in 9Cr-ODS ferritic steels, Mater. Sci. Eng. 527 (2010) 4418–4423.
[21] F.J. Humphreys, M. Hatherly, Recrystallization and Related Annealing Phenomena, second ed., Elsevier, 2004.
[22] K.D. Zilnyk, et al., Martensitic transformation in Eurofer-97 and ODS-Eurofer steels: a comparative study, J. Nucl. Mater. 462 (2015) 360–367.
[23] Y. Ortega, et al., Positron annihilation characteristics of ODS and non-ODS Eurofer isochronally annealed, J. Nucl. Mater. 376 (2008) 222–228.
[24] M. Kolluri, et al., A structure-property correlation study of neutron irradiation induced damage in EU batch of ODS Eurofer97 steel, Mater. Sci. Eng., A 597 (2014) 111–116.
[25] ASTM International, E1245-03: Standard Practice for Determining the Inclusion or Second-phase Constituent Content of Metals by Automatic Image Analysis, 2008, p. 8. USA.
[26] I. Carvalho, H. Schut, A. Fedorov, N. Luzginova, J. Sietsma, Characterization of helium ion implanted reduced activation ferritic/martensitic steel with positron annihilation and helium thermal desorption methods, J. Nucl. Mater. 442 (2013) S48–S51.
[27] R.K. Rehberg, H.S. Leipner, Positron Annihilation in Semiconductors: Defect Studies, Springer, 1999.
[28] H. Schut, A Variable Energy Positron Beam Facility with Applications in Materials Science (doctoral thesis), Delft University of Technology, Delft, NL, 1990.
[29] S. Zhu, M. Yang, X.L. Song, S. Tang, Z.D. Xiang, Characterization of Laves Phase precipitation and its correlation to creep rupture strength of ferritic steels, Mater. Char. 98 (2014) 60–65.
[30] J.S. Lee, H.G. Armaki, K. Maruyama, T. Muraki, H. Asahi, Causes of breakdown of creep strength in 9Cr-1.8W-0.5Mo-VNb steel, Mater. Sci. Eng. 428 (2006) 270–275.
[31] Q. Li, Precipitation of Fe_2W Laves Phase and modelling of its direct influence on the strength of a 12Cr-2W steel, Metall. Mater. Trans. 37A (2006) 89–97.
[32] T. De Nys, P.M. Gielen, Spinodal decomposition in the Fe-Cr system, Metallurgical Transactions 2 (1971) 1423–1428.
[33] J.I. Goldstein, et al., Scanning Electron Microscopy and X-Ray Microanalysis, fourth ed., Springer, 2018.
[34] S. Ukai, S. Mizuta, M. Fujiwara, O. Takanari, T. Kobayashi, Development of 9Cr-ODS martensitic steel claddings for fuel pins by means of ferrite to austenite phase transformation, J. Nucl. Sci. Technol. 39 (7) (2002) 778–788.
[35] S. Mantl, W. Triftshauser, Defect annealing studies on metals by positron annihilation and electrical resistivity measurements, Phys. Rev. B 17 (4) (1978) 1645–1652.
[36] H. Matter, J. Winter, W. Triftshauser, Phase transformations and vacancy formation energies of transition metals by Positron Annihilation, Appl. Phys. 20 (1979) 135–140.
[37] E. del Rio, et al., Formation energy of vacancies in FeCr alloys: dependence on Cr concentration, J. Nucl. Mater. 408 (2011) 18–24.
[38] P. Shewmon, Diffusion in Solids. The Minerals, Metals & Materials Society, second ed., 1989.
[39] H. Mehrer, Diffusion in Solids, first ed., Springer, 2007.
[40] B. Zhang, Calculation of self-diffusion coefficients in iron, AIP Adv. 4 (1) (2014) 1–6.
[41] I. Carvalho, Steels for Nuclear Reactors: Eurofer97, doctoral thesis, Delft University of Technology, Delft, NL, 2016.
[42] M.J.R. Sandim, et al., Coarsening of Y-rich oxide particles in 9% Cr-ODS Eurofer steel annealed at 1350 °C (Short Communication), J. Nucl. Mater. 484 (2017) 283–287. See also references therein.